

Strengthening the magnetic interactions in pseudobinary first-row transition metal thiocyanates, $M(\text{NCS})_2$

Euan N. Bassey,¹ Joseph A. M. Paddison,^{2,3,4} Evan N. Keyzer,¹ Jeongjae Lee,^{1,5} Pascal Manuel,⁶ Ivan da Silva,⁶ Siân E. Dutton,³ Clare P. Grey^{1,*} and Matthew J. Cliffe^{1,7,*}

¹Department of Chemistry, Lensfield Road, University of Cambridge, CB2 1EW, United Kingdom

²Churchill College, University of Cambridge, Storey's Way, Cambridge, CB3 0DS, United Kingdom

³Cavendish Laboratory, Department of Physics, University of Cambridge, JJ Thompson Avenue, Cambridge, CB3 0HE, United Kingdom

⁴Materials Science & Technology Division, Oak Ridge National Laboratory, Oak Ridge, TN 37831, United States of America

⁵School of Earth and Environmental Sciences, Seoul National University, Seoul 08826, Korea

⁶ISIS Facility, STFC Rutherford Appleton Laboratory, Harwell Oxford, Didcot, OX11 0QX, United Kingdom

⁷School of Chemistry, University Park, Nottingham, NG7 2RD, United Kingdom

* To whom correspondence should be addressed;

E-mail: cpg27@cam.ac.uk; matthew.cliffe@nottingham.ac.uk

Understanding the effect of chemical composition on the strength of magnetic interactions is key to the design of magnets with stronger exchange interactions. The magnetic divalent first-row transition metal (TM) thiocyanates are a class of chemically simple layered molecular frameworks. Here, we report two new members of the family, manganese (II) thiocyanate, $\text{Mn}(\text{NCS})_2$, and iron (II) thiocyanate, $\text{Fe}(\text{NCS})_2$. Using magnetic susceptibility measurements on these materials and on cobalt (II) thiocyanate and nickel (II) thiocyanate, $\text{Co}(\text{NCS})_2$ and $\text{Ni}(\text{NCS})_2$, respectively, we identify significantly stronger net antiferromagnetic interactions between the earlier TM ions—a decrease in the Weiss constant, θ , from 29 K for $\text{Ni}(\text{NCS})_2$ to -115 K for $\text{Mn}(\text{NCS})_2$ —a consequence of more diffuse $3d$ orbitals, increased orbital overlap and increasing numbers of unpaired t_{2g} electrons. We elucidate the magnetic structures of these materials: $\text{Mn}(\text{NCS})_2$, $\text{Fe}(\text{NCS})_2$ and $\text{Co}(\text{NCS})_2$ order into the same antiferromagnetic commensurate ground state, whilst $\text{Ni}(\text{NCS})_2$ adopts a ground state structure consisting of ferromagnetically ordered layers stacked antiferromagnetically. We show that magnetic molecular frameworks with significantly stronger net exchange interactions can be constructed by using earlier TMs.

I INTRODUCTION

The rational design and synthesis of new magnetic materials tailored to particular functions requires an understanding of the fundamental interactions taking place between magnetic centres. Magnetic molecular framework materials—that is, systems in which magnetic centres are connected *via*

molecular ligands into lattices—present an excellent opportunity to study these interactions and their chemical origins.

Connecting paramagnetic metal centres with molecular bridging ligands can produce open, flexible structures, permitting potential applications such as multiferroics,^{1–3} magnetostrictive materials⁴ and magnetic sensors.^{5–7} The properties of molecular frameworks are not

determined by long-range electrostatic forces—as in oxide frameworks—but are instead dominated by short-range covalent bonds between the metal centre, M and its ligands, L . The nature and delocalisation of the $M-L$ bond controls the exchange interactions and therefore the magnetic

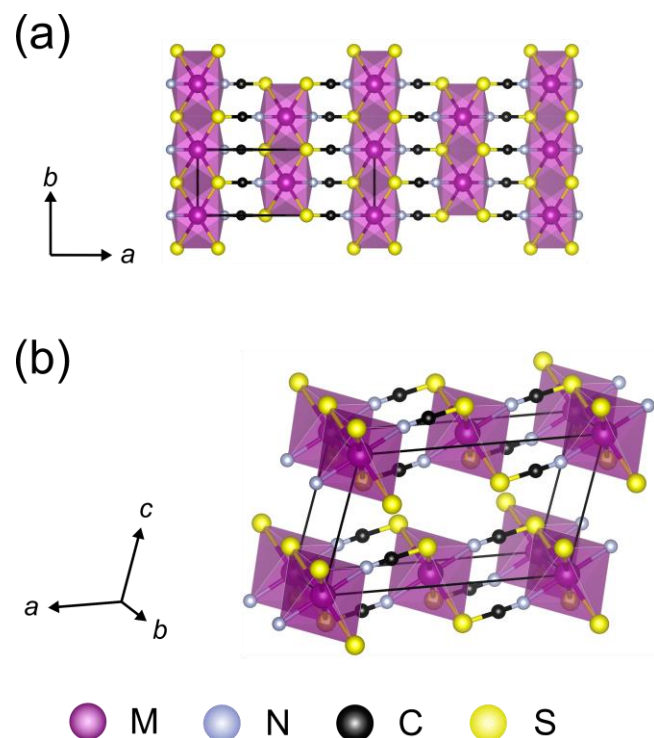


Fig. 1: (a) Projection of a $(2 \times 2 \times 1)$ supercell of $M(\text{NCS})_2$ ($M = \text{Mn, Fe, Co, Ni}$) down the c axis, highlighting the layers of edge- and corner-sharing M^{2+} octahedra. (b) The monoclinic unit cell (space group $C2/m$), as reported in refs. ¹⁷ and ²⁴.

properties of the material. By careful choice of L , very anisotropic structures can be created, which may have low-dimensional magnetic properties.^{8–12}

Low dimensional magnetic materials are examples of many-body quantum systems amenable to exact mathematical treatment.¹³ In particular, the study of the behaviour of low-dimensional magnets is of critical importance to understanding spin-liquids^{14,15} and high-temperature superconductivity.¹⁶

Thiocyanate, $(\text{NCS})^-$, is a promising ligand in magnetic molecular frameworks, as it is capable of promoting strong superexchange interactions between paramagnetic metal centres^{8,17,18}—for example, $J = -230$ K in $\text{Cu}_2(\text{NCS})_4(\text{bpm})$ ($\text{bpm} = 2,2$ -bipyrimidine)¹⁹; it can also generate low-dimensional magnetic materials.^{17,20–22} However, many of the frameworks studied thus far incorporate ancillary ligands, such as acetone,

THF or pyridine, which block coordination sites on the metal and decrease metal-metal connectivity in the framework. This can decrease the net strength of interactions (as measured by the Weiss constant, θ) between paramagnetic centres.^{17,20}

Despite the range of complex magnetic thiocyanate compounds reported,²³ the parent pseudobinary system $M(\text{NCS})_2$ is relatively unexplored, with only three known magnetic examples: $\text{Co}(\text{NCS})_2$,¹⁷ $\text{Ni}(\text{NCS})_2$,^{24,25} and $\text{Cu}(\text{NCS})_2$.⁸ Unlike $\text{Co}(\text{NCS})_2$ and $\text{Ni}(\text{NCS})_2$ —which exhibit a sharp change in magnetic susceptibility at T_N , suggestive of a bulk three-dimensional magnetic ordering transition— $\text{Cu}(\text{NCS})_2$ additionally shows a broad peak, indicative of low-dimensional magnetism.⁸ Indeed, the magnetic lattice of $\text{Cu}(\text{NCS})_2$ is quasi-one-dimensional, comprising an array of weakly coupled antiferromagnetic spin chains, with strong superexchange interactions along the chain ($J = 133$ K), due to the Jahn-Teller distortion of the Cu^{2+} ions.⁸

Previous work has established that both $\text{Co}(\text{NCS})_2$ ¹⁷ and $\text{Ni}(\text{NCS})_2$ ²⁵ also order antiferromagnetically, with Néel ordering temperatures, T_N , of 22 K and 52 K, respectively. The value of θ for $\text{Ni}(\text{NCS})_2$, however, suggested net ferromagnetic interactions ($\theta = 39.8$ K),²⁵ in contrast, $\text{Co}(\text{NCS})_2$ has net antiferromagnetic interactions ($\theta = -40$ K).¹⁷ Understanding the differences between these materials' magnetic behaviours requires an understanding of the interactions taking place in the lattice, which may be inferred from their magnetic structures. At present, the magnetic structures of $\text{Co}(\text{NCS})_2$ and $\text{Ni}(\text{NCS})_2$ are unknown.

The structures adopted by $M(\text{NCS})_2$ are closely-related and directly analogous to the corresponding TM halides, MX_2 , as both series of materials comprise triangular arrays of TM cations stacked along the c axis [Fig. 1].

MX_2 consist of layers of edge-sharing M^{2+} octahedra with weak Van der Waals interactions between the layers [Fig. 1].^{17,24} The triangular arrangement of paramagnetic metal centres in MX_2 , and indeed other magnetic TM oxides^{26–28}, lends itself to geometrically frustrated antiferromagnetic interactions,²⁹ leading to unusual magnetic properties. For example, the divalent TM halides, MX_2 , display multiferroic behaviour and helimagnetism.^{30–33}

In $M(\text{NCS})_2$ ($M = \text{Co}, \text{Ni}$), the magnetic lattice described by the metal centres in the $M(\text{NCS})_2$ layers is the anisotropic triangular lattice, and so $M(\text{NCS})_2$ have the potential to show unusual magnetic behaviour akin to MX_2 . The two

S–M chains (along the [010] direction), and J_2 , between them [Fig. 2(b) and (c)]; the Hamiltonian for this system may be written as:

$$\hat{H} = \sum_{i,j} \mathbf{s}_i J_{ij} \mathbf{s}_j, \quad (1)$$

where the summation is taken over all nearest-neighbour spins i and j with a Heisenberg exchange constant J_{ij} between them.

The spatially anisotropic triangular lattice may be characterised using a single parameter, $\phi = \tan^{-1}\left(\frac{J_1}{J_2}\right)$ [Fig. 2(a)]. By varying the relative Heisenberg exchange interaction strengths, J_1 and J_2 , the isotropic triangular lattice ($J_1 = J_2$) can be transformed into a square lattice, *via* a quasi-one-dimensional chain. In this phase diagram, antiferromagnetic interactions are represented by positive J_i and ferromagnetic by negative J_i . Furthermore, by adding the effect of quantum fluctuations to the classical phase diagram, the magnetic structures of quantum materials—such as the well-known spin-liquid $\text{Cs}_2\text{CuCl}_{4-x}\text{Br}_x$ —may be described.^{34–36}

As thiocyanate is a ‘pseudohalide’,³⁷ we aimed to prepare and characterise molecular framework analogues of the divalent TM halides, to survey the classical two-dimensional magnetic phase diagram through varying the control parameter ϕ .

In this work, we synthesised and characterised $M(\text{NCS})_2$ ($M = \text{Mn}, \text{Fe}, \text{Co}$ and Ni)— $M = \text{Mn}$ and Fe for the first time. Powder X-ray diffraction, thermogravimetric analysis and diffuse reflectance spectroscopy were performed, the latter being used to understand the electronic structures of these materials. In addition, we characterised their magnetic properties using magnetic susceptibility measurements and powder neutron diffraction (PND) and determined the relative sizes of their magnetic exchange interactions.

The results show that the net strength of superexchange interactions, as measured by the Weiss constant, θ , increases and becomes increasingly antiferromagnetic (more negative) as we move to earlier first-row TM cations.

From PND measurements, $\text{Mn}(\text{NCS})_2$, $\text{Fe}(\text{NCS})_2$ and $\text{Co}(\text{NCS})_2$ are observed to adopt the same commensurate magnetic ground state with ordering vector $\mathbf{k} = [100]^*$ and a magnetic stripe ordered structure. In contrast, $\text{Ni}(\text{NCS})_2$ adopts a ground state magnetic structure with ordering

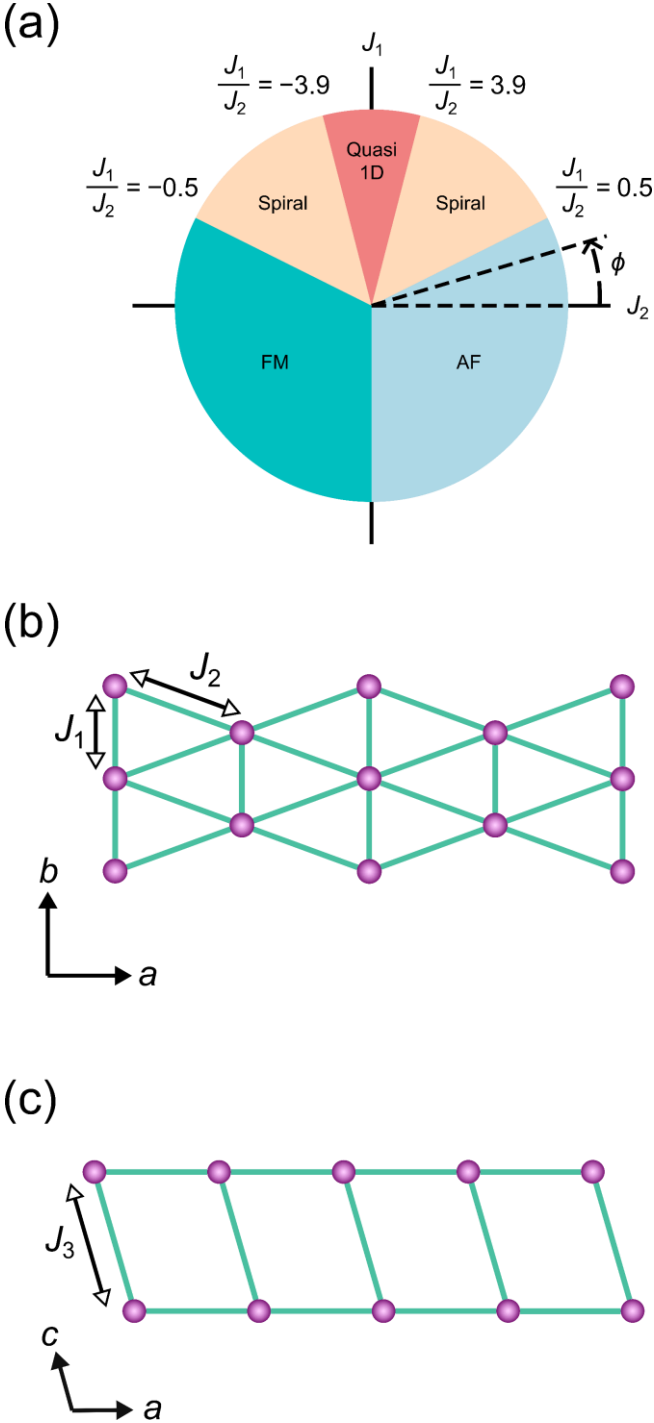


Fig. 2: (a) Classical magnetic phase diagram—i.e. the phase diagram obtained by considering the classical energies of different magnetic lattices—for a two-dimensional triangular lattice with Heisenberg exchange interactions J_1 and J_2 , as illustrated in (b). The interlayer coupling constant, J_3 , for the $M(\text{NCS})_2$ lattice is illustrated in (c). Figure adapted from ref. ³⁴.

interactions within the layers are J_1 , along the M –

vector $k = \left[00\frac{1}{2}\right]^*$, consistent with its very different (and positive) Weiss constant.

II MATERIALS AND METHODS

A. Synthesis

Mn(NCS)₂. MnSO₄·H₂O (Sigma Aldrich, 99%, 1.690 g, 10.00 mmol) was dissolved in the minimum volume of deionised H₂O to yield a pale pink solution. A saturated solution of Ba(SCN)₂·3H₂O (Alfa Aesar, 98%, 3.075 g, 10.00 mmol) was added to this in portions, forming a white precipitate immediately. The reaction mixture was stirred overnight and the precipitate isolated by centrifugation and then decanting the supernatant liquor. The solvent was removed *in vacuo* to yield a yellow residue, which was dried by heating in air at 120°C for one hour before further drying under dynamic vacuum for 48 hours at 100°C. Manganese (II) thiocyanate (1.460 g, 6.01 mmol, 60%) was collected as a pale yellow microcrystalline powder. The same procedure—with all quantities scaled up by a factor of 6.5—was used to synthesise the sample used for neutron diffraction measurements. This compound readily hydrates in ambient humidity, turning from pale yellow to green; as such, it was stored in a dry argon atmosphere.

The product was analysed for elemental purity (combustion analysis for CHN). Found (calculated) C₂N₂S₂Mn: C 13.32% (14.04%), H 0.05% (0.00%), N 15.32% (16.37%).

Fe(NCS)₂. KSCN (Sigma Aldrich, 99%, 0.117 g, 1.2 mmol) was dissolved in dry acetonitrile (approximately 20 cm³) and the clear colourless solution stirred under a nitrogen atmosphere at room temperature. The solution was added to Fe(BF₄)₂·6H₂O (Aldrich, 97%, 0.203 g, 0.6 mmol), instantly forming a dark red solution. The reaction mixture was stirred under a nitrogen atmosphere at room temperature for approximately five minutes, separating to a dark red solution and white precipitate (coloured red by the strongly-coloured supernatant liquor). The mixture was filtered *via* a cannula and the supernatant liquor taken to dryness *in vacuo* to yield a dark red-purple residue, which was heated under dynamic vacuum to form an orange-brown powder. Iron(II) thiocyanate (0.047 g, 0.27 mmol, 45%) was isolated as an orange-brown microcrystalline powder. The same procedure—with all reagent

masses scaled up by a factor of 33—was used to synthesise the sample used for neutron diffraction measurements. The compound is air sensitive, oxidising to form a dark brown powder; as such, the compound was stored under inert atmosphere.

The product was analysed for elemental purity (combustion analysis for CHN). Found (calculated) C₂N₂S₂Fe: C 13.60% (13.97%), H 0.10% (0.00%), N 15.39% (16.29%).

Co(NCS)₂. Adapted from the synthesis detailed in ref. ¹⁷. CoSO₄·7H₂O (Sigma Aldrich, 99%, 2.811 g, 10.00 mmol) was dissolved in the minimum volume of deionised H₂O to generate a clear red solution. A saturated solution of Ba(SCN)₂·3H₂O (Alfa Aesar, 98%, 3.075 g, 10.00 mmol) in deionised H₂O was added in portions, instantly forming a white precipitate, coloured by the strong red supernatant liquor. The reaction mixture was left to stir at room temperature overnight, and the precipitate isolated by centrifugation and then decanting the supernatant liquor. The supernatant liquor was dried *in vacuo*, generating a red-brown residue, which was further dried by heating in air at approximately 120°C for one hour. Cobalt (II) thiocyanate (1.257 g, 7.18 mmol, 72%) was collected as a red-brown microcrystalline powder. The same procedure—with all quantities scaled up by a factor of 6.5—was used to synthesise the sample used for neutron diffraction measurements.

Ni(NCS)₂. NiSO₄·6H₂O (Alfa Aesar, 99.97%, 2.628 g, 10.00 mmol) was dissolved in the minimum volume of deionised H₂O, forming a clear green solution. To this, a saturated solution of Ba(SCN)₂·3H₂O (Alfa Aesar, 98%, 3.075 g, 10.00 mmol) in deionised H₂O was added, instantly forming a white precipitate, coloured green by the supernatant liquor. The reaction mixture was stirred at room temperature overnight and the precipitate removed with a centrifuge. The liquor was dried *in vacuo* to generate a green-brown microcrystalline powder. Nickel (II) thiocyanate (1.501 g, 8.58 mmol, 86%) was collected as a green-brown microcrystalline powder. The same procedure—with all quantities scaled up by a factor of 6.5—was used to synthesise the sample used for neutron diffraction measurements.

B. Powder X-Ray Diffraction (PXRD)

Phase purity was assessed via powder diffraction measurements on a PANalytical Empyrean Diffractometer using Cu-K α radiation ($\lambda = 1.541 \text{ \AA}$)

in Bragg-Brentano geometry. Diffraction patterns were recorded over the range $2\theta = 5\text{--}80^\circ$ using a step size of 0.02° and a scan speed of $0.01^\circ \text{ s}^{-1}$. Due to their sensitivity to moisture and air, the diffraction patterns of $\text{Mn}(\text{NCS})_2$ and $\text{Fe}(\text{NCS})_2$ were measured by encasing the samples between polyimide (Kapton) films. All diffraction patterns were analysed via Pawley³⁸ and Rietveld^{39,40} refinements using TOPAS Academic 6 structure refinement software.^{41,42}

C. Diffuse Reflectance Spectroscopy

Diffuse reflectance spectra were recorded on an Agilent Technologies UV-VIS spectrometer, connected via optical fibre to a Cary 50 Diffuse Reflectance Accessory, using a wavelength range $\lambda = 200 - 1000 \text{ nm}$, with step size 1.00 nm and scan rate of 10 nm s^{-1} . Samples were loaded between two quartz discs and sealed with Parafilm. Samples of $\text{Mn}(\text{NCS})_2$ and $\text{Fe}(\text{NCS})_2$ were mounted onto the quartz discs inside an argon-filled glovebox and quickly transported to the spectrometer (within half an hour) for analysis. $\text{Mn}(\text{NCS})_2$ was diluted with BaSO_4 powder in a 1:1 mass ratio and the mixture ground together to produce a homogeneous powder; $\text{Fe}(\text{NCS})_2$, $\text{Co}(\text{NCS})_2$ and $\text{Ni}(\text{NCS})_2$ were mixed in 1:10 ($\text{M}(\text{NCS})_2$: BaSO_4) mass ratios and the mixture ground together to produce homogeneous powders. The spectra were averaged over multiple measurements; spikes in the average due to erroneous spikes in the raw data—i.e. spikes in one spectrum which do not repeat in the other spectra, likely due to specular reflection from the powder—were removed from the average and the 'spiked' data point replaced with the average intensity either side of the spike.

D. Thermogravimetric Analysis (TGA)

Thermogravimetric data for $\text{Mn}(\text{NCS})_2$, $\text{Co}(\text{NCS})_2$ and $\text{Ni}(\text{NCS})_2$ were recorded with a Mettler-Toledo Thermogravimetric Analysis/Simultaneous Differential Thermal Analysis (TGA/SDTA) 851 Thermobalance. Each powder sample (20 – 50 mg) was loaded into an alumina crucible and heated from 50°C to 600°C at a heating rate of $10^\circ\text{C min}^{-1}$ under a nitrogen atmosphere. The data collected was measured relative to a background blank TGA curve, recorded using the same alumina crucible, temperature range and heating rate, under a nitrogen atmosphere.

E. Magnetic Susceptibility Measurements

The magnetic susceptibility measurements were carried out on powder samples (10 – 20 mg) using a Quantum Design Magnetic Property Measurement System 3 (MPMS) superconducting quantum interference device (SQUID) magnetometer. The zero-field cooled (ZFC) and field-cooled (FC) susceptibilities were measured in a field of 0.01 T over a temperature range 2 – 300 K. As $M(H)$ is linear in this field range, the small-field approximation to the susceptibility, $\chi \approx \frac{M}{H}$, was assumed to be valid. The data for each compound were corrected for diamagnetism of the sample using Pascal's constants.⁴³

F. Powder Neutron Diffraction (PND)

Powder neutron diffraction measurements were carried out at the ISIS Pulsed Neutron and Muon Source using the WISH ($\text{Mn}(\text{NCS})_2$, $\text{Co}(\text{NCS})_2$, $\text{Ni}(\text{NCS})_2$) and GEM ($\text{Fe}(\text{NCS})_2$) instruments.⁴⁴ Samples of $\text{Mn}(\text{NCS})_2$ (4.76 g), $\text{Fe}(\text{NCS})_2$ (2.26 g), $\text{Co}(\text{NCS})_2$ (2.44 g) and $\text{Ni}(\text{NCS})_2$ (4.76 g) were loaded into thin-walled vanadium canisters. The canister diameters were 11 mm for $\text{Mn}(\text{NCS})_2$ and $\text{Ni}(\text{NCS})_2$; 6 mm for $\text{Co}(\text{NCS})_2$ and 6 mm with an indium seal for $\text{Fe}(\text{NCS})_2$. Each sample was loaded to a height of at least 40 mm, to ensure the full beam illuminates the sample.

Each sample was first cooled to the base temperature (1.5 K for $\text{Mn}(\text{NCS})_2$, $\text{Co}(\text{NCS})_2$ and $\text{Ni}(\text{NCS})_2$ and 10 K for $\text{Fe}(\text{NCS})_2$) and diffraction patterns then collected at a series of temperatures through T_N . The complete list of temperature steps and data collections may be found in the supporting information. The data were corrected for absorption effects using the Mantid software package.⁴⁵

For each structure, the nuclear structure was determined by Rietveld refinement against powder neutron diffraction data collected above T_N , using a model derived from the previously reported single crystal structure of $\text{Ni}(\text{NCS})_2$.²⁴ All refinements were carried out using Topas Academic 6.0.⁴²

Rietveld refinements using the candidate magnetic irreducible representations (irreps) were carried out for each compound separately, which showed that in each case only one of the two single irrep structures was consistent with the experimental data. Including the second irrep did not significantly improve the fit to the data. On this basis, we refined the magnetic structures using

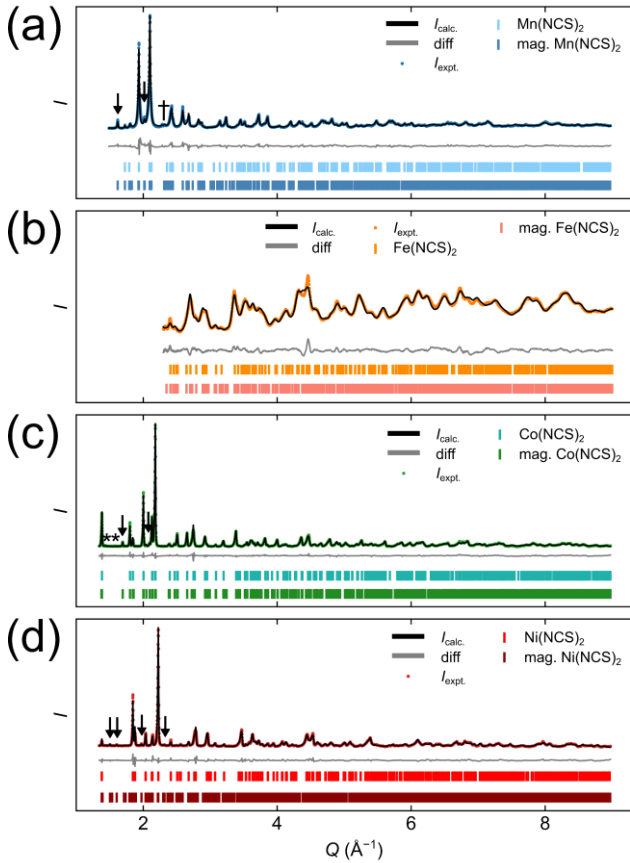


Fig. 3: Rietveld refinements of the neutron powder diffraction patterns collected at 1.5 K for $\text{Mn}(\text{NCS})_2$, (a); at 1.5 K for $\text{Co}(\text{NCS})_2$, (c) and 1.5 K for $\text{Ni}(\text{NCS})_2$ (d), all on Bank 5 of WISH. (b) shows the pattern collected at 10 K for $\text{Fe}(\text{NCS})_2$ on Bank 5 of GEM. Arrows denote magnetic peaks, asterisks denote magnetic reflections from impurity phases, whilst daggers denote non-magnetic reflections from impurity phases. $R_{\text{wp}} = 7.542\%$ for $\text{Mn}(\text{NCS})_2$, 3.303% for $\text{Fe}(\text{NCS})_2$, 4.061% for $\text{Co}(\text{NCS})_2$ and 6.253% for $\text{Ni}(\text{NCS})_2$.

only the mY_2^+ irrep for $\text{Mn}(\text{NCS})_2$, $\text{Co}(\text{NCS})_2$ and $\text{Fe}(\text{NCS})_2$, and the mA_1^+ irrep for $\text{Ni}(\text{NCS})_2$. All refinements were carried out by simultaneously refining against data collected on multiple banks of detectors: on WISH, for $\text{Mn}(\text{NCS})_2$, banks 2 – 5; for $\text{Co}(\text{NCS})_2$, banks 1 – 5 and for $\text{Ni}(\text{NCS})_2$, banks 2 – 5; on GEM, for $\text{Fe}(\text{NCS})_2$, banks 2 – 5.

Table 1: Rietveld-derived lattice parameters and atomic coordinates, based on the powder neutron diffraction data collected at 1.5 K for $\text{Mn}(\text{NCS})_2$, 10 K for $\text{Fe}(\text{NCS})_2$, 1.5 K for $\text{Co}(\text{NCS})_2$ and 1.5 K for $\text{Ni}(\text{NCS})_2$. The space group for all compounds is $C2/m$; as such, the α and γ angles were not refined, as these quantities define the monoclinic lattice.

$\text{Mn}(\text{NCS})_2$			
a (Å)	10.8370(17)	α (°)	90
b (Å)	3.8824(6)	β (°)	105.348(2)
c (Å)	6.2175(9)	γ (°)	90
Mn	Site $2a$	x	y z
N	$4i$	0	0 0
C	$4i$	-0.1445(2)	0 0.1723(4)
S	$4i$	-0.2465(4)	0 0.2278(6)
			0 0.2721(11)
$\text{Fe}(\text{NCS})_2$			
a (Å)	10.6068(13)	α (°)	90
b (Å)	3.7327(5)	β (°)	105.043(6)
c (Å)	6.1575(9)	γ (°)	90
Fe	Site $2a$	x	y z
N	$4i$	0	0 0
C	$4i$	-0.14085(11)	0 0.17558(18)
S	$4i$	-0.24005(12)	0 0.2215(3)
			0 0.2700(4)
$\text{Co}(\text{NCS})_2$			
a (Å)	10.6128(2)	α (°)	90
b (Å)	3.70879(7)	β (°)	106.4419(8)
c (Å)	6.14017(11)	γ (°)	90
Co	Site $2a$	x	y z
N	$4i$	0	0 0
C	$4i$	-0.13798(7)	0 0.17044(12)
S	$4i$	-0.23806(11)	0 0.2172(2)
			0 0.2604(4)
$\text{Ni}(\text{NCS})_2$			
a (Å)	10.5026(5)	α (°)	90
b (Å)	3.61884(5)	β (°)	107.514(3)
c (Å)	6.16305(17)	γ (°)	90
Ni	Site $2a$	x	y z
N	$4i$	0	0 0
C	$4i$	-0.1345(3)	0 0.1613(5)
S	$4i$	-0.2362(3)	0 0.2072(7)
			0 0.2277(12)

For the final refinements of the data collected for $\text{Mn}(\text{NCS})_2$ using the WISH diffractometer and for the final refinement of the data collected for $\text{Fe}(\text{NCS})_2$ on the GEM diffractometer, it proved necessary to refine the Voigt peak-shape parameters separately for high Q and low Q data, due to their unusual Q -dependence.

For all refinements, the lattice parameters, atomic positions and the magnitudes and directions of the magnetic moments were allowed to refine freely, aside from restraints on the C–N (ca. 1.15 Å) and C–S (ca. 1.65 Å) bond lengths. For $\text{Mn}(\text{NCS})_2$, $\text{Fe}(\text{NCS})_2$ and $\text{Co}(\text{NCS})_2$, the same set of freely refining anisotropic atomic displacement

parameters was used for each atom. A full structural refinement for Ni(NCS)₂ using anisotropic atomic displacement parameters was not possible and an isotropic displacement parameter for each atom was used. In all cases, the bond lengths and angles were consistent with those expected from previous studies [Table S1].^{17,24}

III RESULTS

A. Bulk characterisation

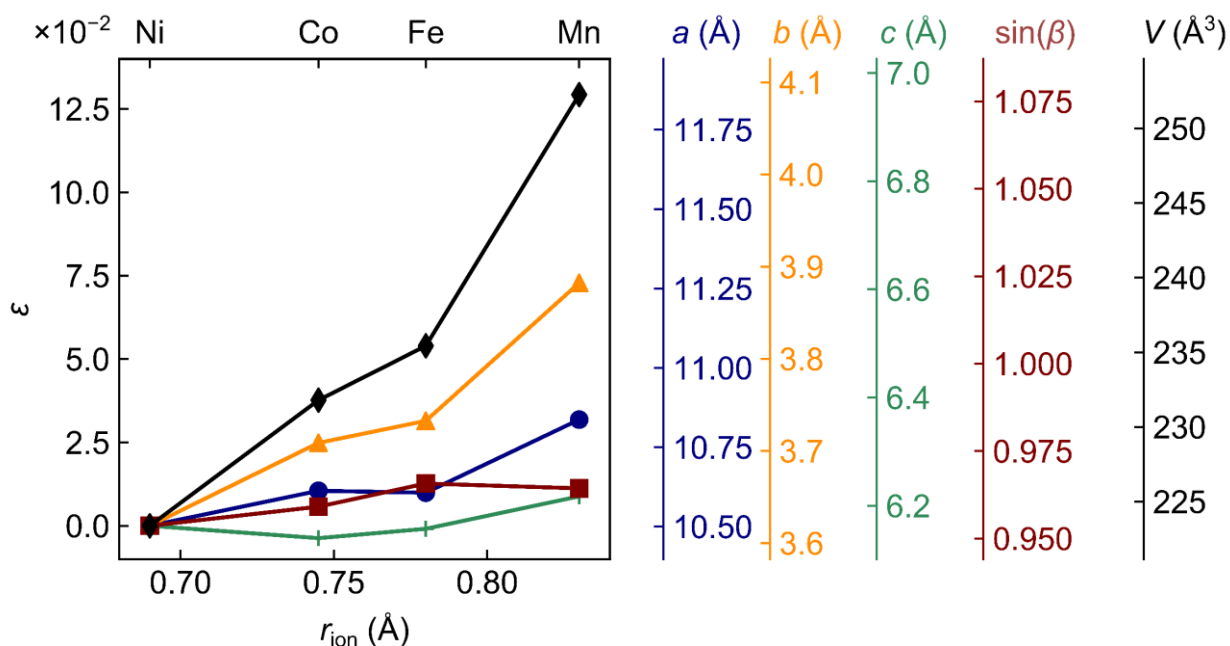


Fig. 4: Variation in the strain of Rietveld-derived PND lattice parameters and nuclear unit cell volume (at the base temperature of PND results) with the ionic radius of M^{2+} , r_{ion} . The strain in each parameter, x , is calculated via $\epsilon = \frac{x - x_{Ni}}{x_{Ni}}$ – i.e. the strain is calculated relative to the parameters obtained for Ni(NCS)₂. The values used to calculate the strain are shown on the right hand axes.

The $M(NCS)_2$ family members ($M = Mn^{2+}$, Fe^{2+} , Co^{2+} , Ni^{2+}) were synthesised *via* metathesis reactions, driven by precipitation of an insoluble side-product ($BaSO_4$ for $M = Mn$, Co , Ni ; KBF_4 for $M = Fe$). Apart from Ni(NCS)₂, all compounds crystallised as solvates; the co-crystallised solvent was removed by heating either *in vacuo* ($M = Fe$, Mn) or in air ($M = Co$).

To confirm that no solvent remained trapped in the synthesised frameworks, we carried out thermogravimetric analysis (TGA) [Fig. S1]. This showed no mass losses other than minimal quantities of surface water, as suggested by the low quantity of H determined *via* elemental analysis. Quantitative Rietveld refinements of the high-Q powder neutron diffraction (PND) data

collected confirmed that all four compounds were isostructural [Fig. 3], crystallising in the space group $C2/m$, as anticipated for the similar chemistries and ionic radii of the divalent first row TM cations,⁴⁶ with only minor levels of impurities detected. For Co(NCS)₂, the impurity phase was unreacted $CoSO_4 \cdot 6H_2O$ (1 wt.%), whilst the impurity in Mn(NCS)₂ could not be assigned or quantified. Fe(NCS)₂ appeared much less crystalline than the other samples, likely due to the rapid removal of solvent during crystallisation. Consequently, the errors in the parameters

extracted from Rietveld refinements of the Fe(NCS)₂ PND patterns are larger than for other members of the $M(NCS)_2$ family; we believe these parameters are still meaningful, despite the larger errors.

The lattice parameters and atomic coordinates derived from Rietveld refinements are shown in Table 1. The lattice parameters and unit cell volume vary approximately linearly with cationic radius, r_{ion} [Fig. 4]. Among the lattice parameters, b increased the most, followed by a and then c .

The b lattice parameter depends only on the $M-S$ bond lengths and $M-S-M$ bond angle and therefore changes proportionately the most. The observed changes in b are also consistent with the

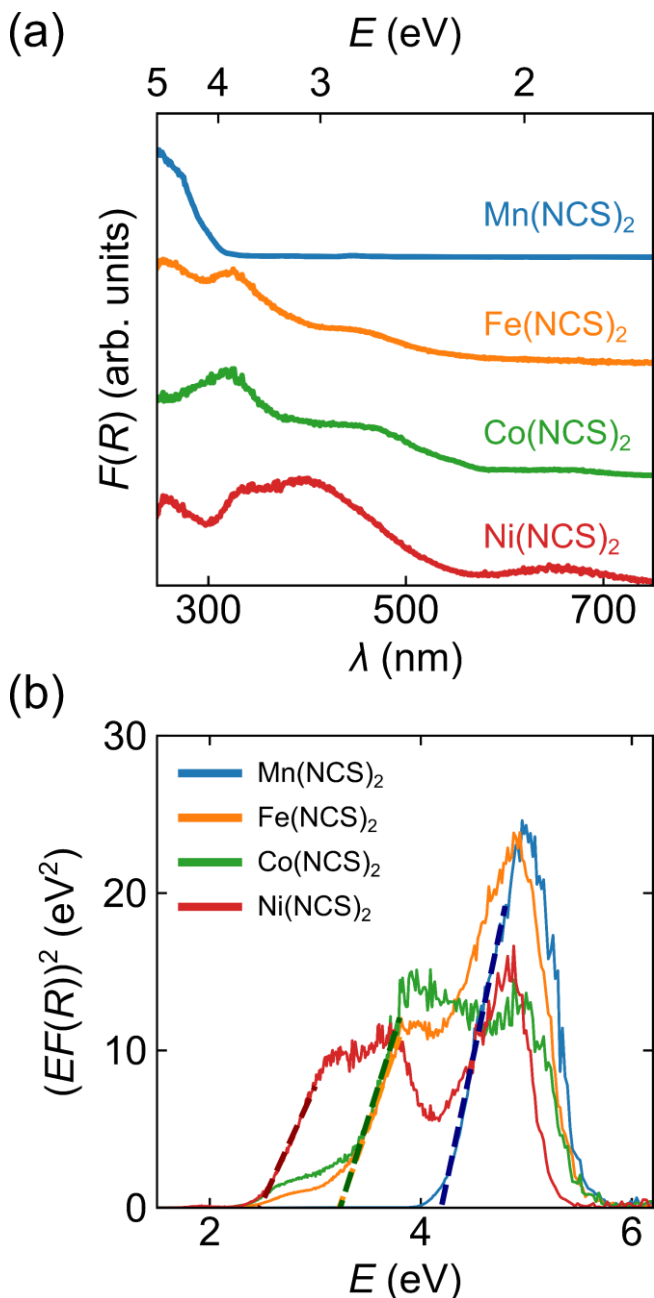


Fig. 5: (a) Diffuse reflectance spectra for $M(\text{NCS})_2$ ($M = \text{Mn, Fe, Co, Ni}$). (b) Tauc plots of the diffuse reflectance data: extrapolation of the data to $(F(R)hv)^2 = 0$ (indicated by the dashed line) yields the band gap for each material.

expected differences in M -S bond lengths across the TM series.

The value of the a lattice parameter is dominated by the length of $(\text{NCS})^-$ anion, as it lies along the a axis, rather than the N-M and M -S bonds, which are oriented at an angle to the a direction [Fig. 1]. Since the length of $(\text{NCS})^-$ remains near constant regardless of the identity of M , changes in M have a small effect on the size of a . The c lattice parameter is determined by the interlayer Van der Waals interactions, which likewise remain

approximately constant across the first-row TM series.

All compounds except $\text{Mn}(\text{NCS})_2$ were strongly coloured microcrystalline powders: $\text{Fe}(\text{NCS})_2$ was orange-brown, $\text{Co}(\text{NCS})_2$ was red-brown¹⁷ and $\text{Ni}(\text{NCS})_2$ green-brown; $\text{Mn}(\text{NCS})_2$ was pale yellow.²⁴

We used diffuse reflectance UV-Vis spectroscopy to quantitatively assess the variation in observed colours across the $M(\text{NCS})_2$ series [Fig. 5(a)].

Previous work on $(\text{NCS})^-$ frameworks has suggested that transitions in the observed diffuse reflectance spectra correspond to ligand-to-metal charge transfer (LMCT) transitions, from states dominated by $(\text{NCS})^-$ -based orbitals to states dominated by the metal $3d$ orbitals.^{47–49} The additional weak absorption bands observed for $\text{Fe}(\text{NCS})_2$, $\text{Co}(\text{NCS})_2$ and $\text{Ni}(\text{NCS})_2$ likely correspond to d - d transitions.⁵⁰ The optical (indirect) band gaps were extracted using Tauc fits

Table 2: Bulk magnetic susceptibility parameters, extracted from the raw magnetic susceptibility data (T_N), high-temperature Curie-Weiss law fits (θ , μ_{eff} and g) and the staggered moments, $m_{\text{sta.}}$, of each material, obtained from Rietveld refinement of the low temperature PND data. Experimental standard errors are given in parentheses.

	$\text{Mn}(\text{NCS})_2$	$\text{Fe}(\text{NCS})_2$	$\text{Co}(\text{NCS})_2$	$\text{Ni}(\text{NCS})_2$
θ (K)	-115(3)	-78(3)	-44(1)	+29(1)
T_N (K)	28.0(3)	78.4(3)	20.0(5)	54(2)
μ_{eff} (μ_B)	6.44(5)	6.19(6)	4.44(4)	2.79(2)
g	2.18(2)	2.53(2)	2.29(2)	1.97(1)
$m_{\text{sta.}}$ (μ_B)	4.02(4)	4.82(6)	3.02(2)	1.75(5)

to the data,⁵¹ giving the following values: 4.2(1) eV for $\text{Mn}(\text{NCS})_2$, 3.2(1) eV for $\text{Fe}(\text{NCS})_2$, 3.2(1) eV for $\text{Co}(\text{NCS})_2$ and 2.5(1) eV for $\text{Ni}(\text{NCS})_2$.

On moving to later TM ions, the d orbitals decrease in energy and the crystal field splitting increases, resulting in a lower energy (longer wavelength) transition and smaller band gap. This trend is consistent with the small observed band gap for $\text{Cu}(\text{NCS})_2$ (1.3 eV), which is lowered further due to Jahn-Teller distortions of the Cu^{2+} ions.⁸

B. Bulk magnetic measurements

To assess the change in the magnetic properties as the identity of M in $M(\text{NCS})_2$ varies, we next went on to measure the bulk magnetic susceptibilities of these compounds at $H = 0.01$ T [Fig. 6].

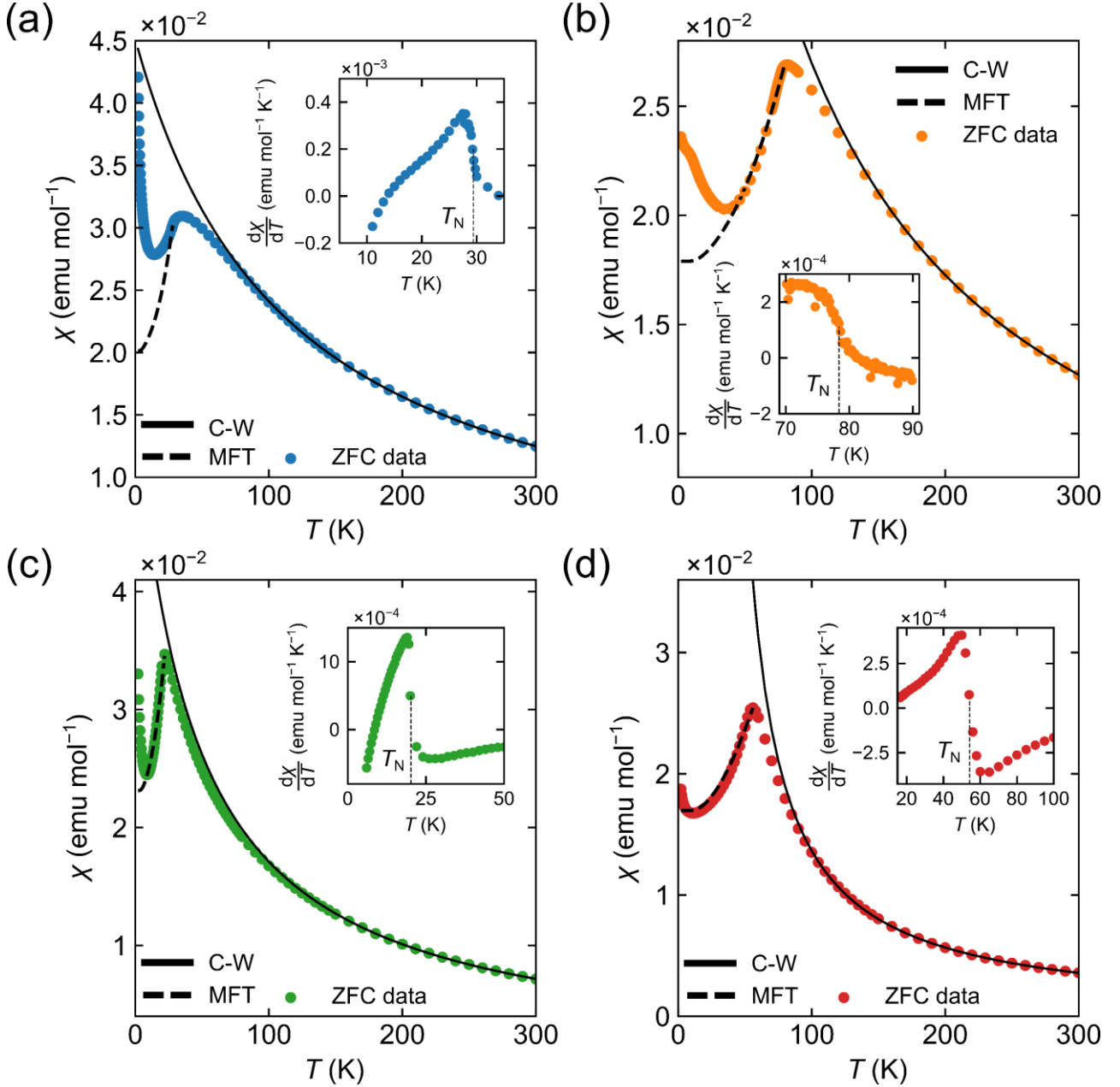


Fig. 6: Zero-field cooled (ZFC) magnetic susceptibility data collected for Mn(NCS)_2 (a), Fe(NCS)_2 (b), Co(NCS)_2 (c) and Ni(NCS)_2 (d) in a constant magnetic field strength $H = 100$ Oe. The Curie-Weiss law was used to model the high-temperature ($T > 150$ K) data, while a low-temperature mean-field theory (MFT) model was used for the data $T < T_N$. Insets show the first field derivative of magnetic susceptibility, used to identify magnetic phase transitions.

All four compounds showed evidence of three-dimensional antiferromagnetic ordering [Fig. 6]: a sharp change in $\frac{d\chi}{dT}$ at the Néel temperature, T_N [Insets of Fig. 6], and a rapid decrease in χ at low temperatures. Each compound also shows a rise in the susceptibility at low temperatures ($T < 15$ K for $M = \text{Fe, Co, Ni}$ and $T < 35$ K for $M = \text{Mn}$), due to small (non-quantifiable) amounts of paramagnetic impurities and defects.

For each compound, the high-temperature ($T > 150$ K) data were fitted to the Curie-Weiss law, yielding values of the Weiss constant, θ , and Curie constant, C . The values of θ are presented in Table

2, alongside T_N and the effective magnetic moments, μ_{eff} , and g -factors, g (where $g = \frac{\mu_{\text{eff}}}{\sqrt{S(S+1)}}$).

The data collected for Ni(NCS)_2 and Co(NCS)_2 are broadly consistent with measurements previously reported, with values of T_N differing only slightly from those reported in previous work.^{17,25}

The g -values are also broadly consistent with previously reported g -values—for Co(NCS)_2 , $g \approx 2.36$;¹⁷ for Ni(NCS)_2 , $g \approx 2.13$.²⁵

The large deviations in μ_{eff} from the spin-only values (i.e. $\mu_{\text{eff}} = 2\sqrt{S(S+1)}$) for Fe(NCS)_2 and Co(NCS)_2 arise from spin-orbit coupling, due to the

residual orbital angular momentum in the ${}^5T_{2g}$ and ${}^4T_{1g}$ terms for high-spin octahedral Fe^{2+} and Co^{2+} , respectively.^{52–55} The deviation for $\text{Mn}(\text{NCS})_2$ is smaller than for $\text{Fe}(\text{NCS})_2$ and $\text{Co}(\text{NCS})_2$, as Mn^{2+} carries no orbital angular momentum—i.e. $L =$

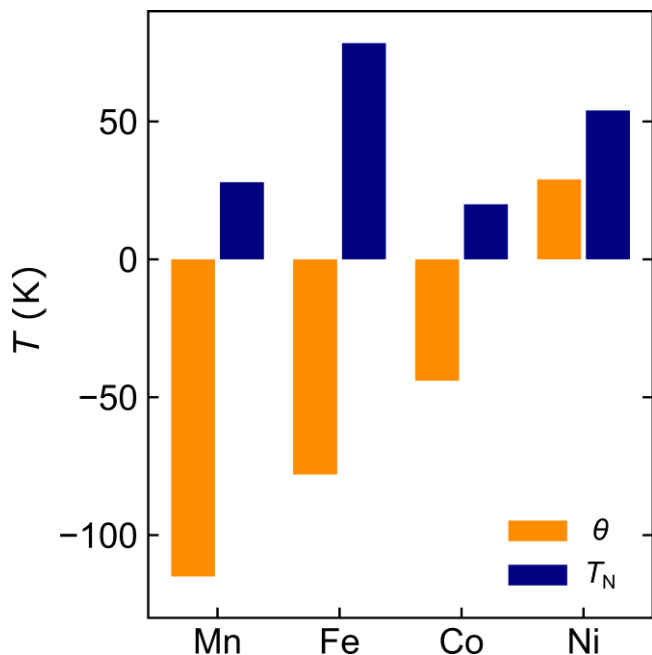


Fig. 7: Variation of the Weiss temperature, θ , and Néel Temperature, T_N , across the first-row transition metals, M , in the $M(\text{NCS})_2$ family.

0.^{56,57} While spin-orbit coupling is expected to increase across the TM series, the spin-orbit coupling is quenched to a first approximation for the d^8 Ni^{2+} (A_{2g}) ion; as such, μ_{eff} for $\text{Ni}(\text{NCS})_2$ closely matches the spin-only value.

The variation of θ across the $M(\text{NCS})_2$ family indicates that the net magnetic interactions become increasingly antiferromagnetic on moving to earlier TM ions [Fig. 7], likely due to the more diffuse nature of M^{2+} $3d$ orbitals earlier in the series, enabling better spatial overlap with the thiocyanate σ and π frontier orbitals.

The Weiss constants determined highlight the considerable increase in the strength of net magnetic interactions between spins on moving to earlier TM ions, particularly for $\text{Mn}(\text{NCS})_2$ and $\text{Fe}(\text{NCS})_2$.

As the $M(\text{NCS})_2$ are layered materials with weak Van der Waals interactions between the layers, we anticipated these materials would display low-dimensional magnetic behaviour. The ratio $f = |\theta|/T_N$ was computed for each compound, as this parameter may be used to assess the extent to which long-range order is suppressed by low-

dimensionality or spin frustration in these materials.¹³ For $\text{Mn}(\text{NCS})_2$, $f = 4.1(1)$; for $\text{Fe}(\text{NCS})_2$, $f = 0.99(4)$; for $\text{Co}(\text{NCS})_2$, $f = 2.2(1)$ and for $\text{Ni}(\text{NCS})_2$, $f = 0.54(3)$, which do not suggest strong suppression of long-range order.¹³

The observed variation in susceptibility below T_N was then modelled using a powder-average mean-field theory (MFT) model with Heisenberg exchange [Fig. 6].^{58,59} This model qualitatively accounted for the observed magnetic susceptibilities, but could not be used to extract the exchange interaction strengths, J_1 , J_2 and J_3 [Fig. 2(b)], as these parameters are correlated. We then attempted to determine the values of J_1 , J_2 and J_3 using a reaction-field model.⁶⁰ However, this again proved unsuccessful, as strong correlations between the parameters again precluded their reliable determination.

To assess whether any field-induced magnetic phase transitions occur in the compounds, isothermal magnetisation measurements ($M(H)$ curves) were carried out [Figs. S2–S5]. The $M(H)$ curves show that, in the region -7 to $+7$ T, saturation is not achieved, and that each material undergoes a spin reorientation transition (at $H = \pm 0.35$ T, ± 1.00 T, ± 1.20 and ± 1.35 T for $M = \text{Mn}$, Fe , Co and Ni , respectively).

C. Magnetic ground state from neutron diffraction experiments

The dominant interactions in the $M(\text{NCS})_2$ frameworks may be understood by examining their ordered magnetic structures. As such, we carried out low-temperature neutron diffraction experiments to determine the magnetic ground state of these frameworks. All four compounds were observed to adopt ordered commensurate ground states.

On cooling $\text{Mn}(\text{NCS})_2$ below T_N ($= 28$ K), superlattice reflections were observed, corresponding to a propagation vector $\mathbf{k} = [100]^*$. Similarly, for $\text{Fe}(\text{NCS})_2$ and $\text{Co}(\text{NCS})_2$, superlattice reflections corresponding to the $\mathbf{k} = [100]^*$ propagation vector were observed below $T_N = 80$ K and 22 K, respectively [Figs. 8(a), 8(b) and 8(c)]; the temperature dependence of these peaks' intensities are shown in the insets of Fig. S6. This propagation vector corresponds to breaking of the lattice C -centring, leading to a primitive magnetic cell which is twice the size of the primitive nuclear cell.

Symmetry-mode analysis was used to determine the symmetry-allowed magnetic irreducible representations (irreps.), yielding mY_1^+ and mY_2^+ irreps, in Miller and Love's notation,⁶¹ for $\text{Mn}(\text{NCS})_2$, $\text{Fe}(\text{NCS})_2$ and $\text{Co}(\text{NCS})_2$. Rietveld

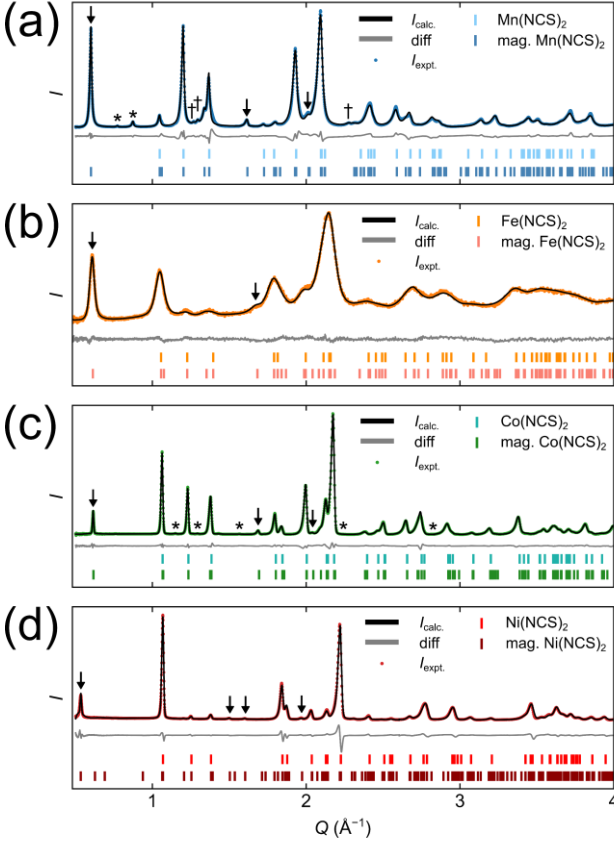


Fig. 8: Rietveld fits to the PND patterns between $Q = 1 \text{ \AA}^{-1}$ and $Q = 4 \text{ \AA}^{-1}$ collected at 1.5 K for $\text{Mn}(\text{NCS})_2$ (a); at 1.5 K for $\text{Co}(\text{NCS})_2$ (c); and $\text{Ni}(\text{NCS})_2$ at 1.5 K (d), all on Bank 2 of WISH. (b) shows the PND pattern for $\text{Fe}(\text{NCS})_2$ collected at 10 K on Bank 2 of GEM. Arrows highlight magnetic reflections from magnetically ordered $M(\text{NCS})_2$; asterisks indicate reflections from magnetic impurities, whilst daggers denote reflections from non-magnetic impurities. $R_{\text{wp}} = 7.542\%$ for $\text{Mn}(\text{NCS})_2$, 3.303% for $\text{Fe}(\text{NCS})_2$, 4.061% for $\text{Co}(\text{NCS})_2$ and 6.253% for $\text{Ni}(\text{NCS})_2$.

refinement of the data using these irreps revealed that only the mY_2^+ irrep was consistent with the data for $\text{Mn}(\text{NCS})_2$, $\text{Fe}(\text{NCS})_2$ and $\text{Co}(\text{NCS})_2$. The refinements against the mY_2^+ symmetry-adapted mode yielded staggered magnetic moments of $4.02(4) \mu_{\text{B}}$ ($\text{Mn}(\text{NCS})_2$), $4.82(6) \mu_{\text{B}}$ ($\text{Fe}(\text{NCS})_2$) and $3.018(16) \mu_{\text{B}}$ ($\text{Co}(\text{NCS})_2$), with magnetic space group $\text{P}A_2/c$ in the BNS notation.⁶²

In contrast to the other members of the $M(\text{NCS})_2$ family, the magnetic Bragg peaks observed below $T_{\text{N}} = 56 \text{ K}$ for $\text{Ni}(\text{NCS})_2$ were indexed to a

propagation vector of $\mathbf{k} = [00\frac{1}{2}]^*$, corresponding to mA_1^+ and mA_2^+ irreps. The neutron diffraction data were consistent with the mA_2^+ -distorted structure and Rietveld refinement against this structure [Fig. 8(d)] yielded a staggered moment of $1.73(5) \mu_{\text{B}}$ and a magnetic space group C_c2/c in the BNS notation, with the magnetic unit cell doubled along the c -direction, relative to the nuclear cell [Fig. 9].

Since $\text{Ni}(\text{NCS})_2$ is ferromagnetic within the layer, we anticipate $J_1/J_2 > -0.5$ and $J_2 < 0$ (i.e. ferromagnetic), so that $\text{Ni}(\text{NCS})_2$ lies in the FM region of the classical phase diagram [Fig. 2(a)]. Likewise, we anticipate $J_1/J_2 < 0.5$ and $J_2 > 0$ for $\text{Mn}(\text{NCS})_2$, $\text{Fe}(\text{NCS})_2$ and $\text{Co}(\text{NCS})_2$, so that these materials occupy the AF region of the classical

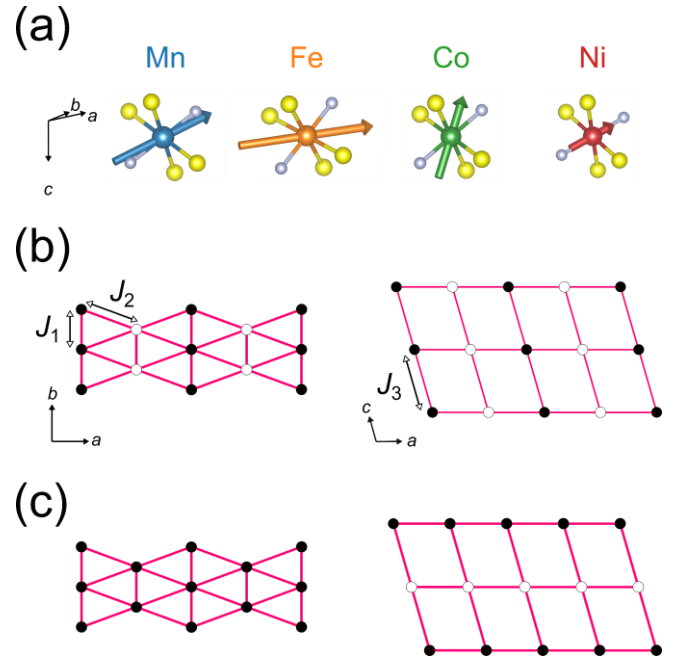


Fig. 9: (a) Schematic of the ordered magnetic moments of Mn^{2+} , Fe^{2+} , Co^{2+} and Ni^{2+} in $M(\text{NCS})_2$ relative to the N–M–N axis (N atoms in grey-blue, S in yellow). The magnetic lattice adopted by $\text{Mn}(\text{NCS})_2$, $\text{Fe}(\text{NCS})_2$ and $\text{Co}(\text{NCS})_2$ is shown in (b), whilst (c) shows the magnetic lattice of $\text{Ni}(\text{NCS})_2$. Filled and empty circles denote collinear moments with opposite spatial orientations.

phase diagram [Fig. 2(a)]. Additional constraints on the relative sizes and signs of J_1 and J_2 are established in the Discussion.

In all cases, the spins in $M(\text{NCS})_2$ are constrained by symmetry to lie in the ac plane. The staggered moments of $\text{Fe}(\text{NCS})_2$, $\text{Co}(\text{NCS})_2$ and $\text{Ni}(\text{NCS})_2$ are broadly consistent with the spin-only moments measured *via* bulk magnetic susceptibility measurements [Table 2], with deviations from the

spin-only values likely arising from spin-orbit coupling and delocalisation (covalency) effects (see Discussion).

We also established the temperature dependence of the lattice parameters [Fig. S7]. For all members of the $M(\text{NCS})_2$ family, the lattice parameters were observed to vary broadly linearly with temperature, with no discontinuities observed.

For $\text{Mn}(\text{NCS})_2$, $\text{Co}(\text{NCS})_2$ and $\text{Ni}(\text{NCS})_2$, the c -axis is observed to expand most as temperature rises [Figs. S7], since the interactions along the c axis are primarily weaker Van der Waals interactions between the layers.

We were unable to accurately determine the temperature dependence of lattice parameters for $\text{Fe}(\text{NCS})_2$ due to lower crystallinity of the sample.

IV DISCUSSION

The family of divalent first-row TM thiocyanates $M(\text{NCS})_2$ ($M = \text{Mn}, \text{Fe}, \text{Co}$ and Ni) adopt the same layered crystal structure, with space group $C2/m$. On changing the identity of M , we observe broadly linear variations in the lattice parameters with the ionic radius of M^{2+} . The changes in local bonding and orbital occupancies will change the strength of magnetic interactions between the nearest neighbour M^{2+} centres, J_1 , J_2 and J_3 . The changes in the individual interaction strengths are reflected in the value of the Weiss constant, θ , which indicates the net interaction strength, accounting for the relative signs of the magnetic interactions in the lattice.

As earlier first-row TM ions occupy the M^{2+} sites in the $M(\text{NCS})_2$ structure, θ becomes increasingly antiferromagnetic [Fig. 7], due to (individually) stronger antiferromagnetic interactions and/or weaker ferromagnetic interactions.

We expect that the magnetic properties of the $M(\text{NCS})_2$ lattices are dominated by the two nearest neighbour superexchange interactions, J_1 and J_2 , as the interlayer interaction, J_3 , is likely weak, due to the large separation of M^{2+} ions and lack of chemical bonds between these ions.

The dipolar interactions between M^{2+} are expected to be small, due to the large distances between M^{2+} centres (at least 3.6 Å, corresponding to a dipolar interaction strength on the order of 0.01 K).

Therefore, we expect the strengths of the dominant exchange interactions in $M(\text{NCS})_2$ to depend primarily on the occupation of the magnetic $3d$ orbitals and their overlap with the frontier orbitals on $(\text{NCS})^-$; direct exchange is expected to be weak, due to the large separation between M^{2+} ions.

The J_1 interaction, corresponding to the interaction in the [010] direction (over the M -S- M linkage) will likely contain two contributions: firstly, antiferromagnetic superexchange involving overlap between t_{2g} and e_g orbitals on adjacent M^{2+} ions (mediated by a S p -like orbital, Fig. 10(a)) and secondly, ferromagnetic exchange-correlation-driven superexchange mediated by the two orthogonal sulphur p -like orbitals [Fig. 10(c)].

The strong exchange correlation on S^{63-65} favours a ferromagnetic J_1 interaction, consistent with ferromagnetic ordering along the [010] direction, as observed in all $M(\text{NCS})_2$ materials by PND. The antiferromagnetic component will weaken from left to right across the TM series, as the number of unpaired electrons in t_{2g} orbitals decreases. For $M = \text{Ni}$, the t_{2g} orbitals are fully occupied and we anticipate no antiferromagnetic component. Consequently, we expect the J_1 interaction to become increasingly ferromagnetic from left to right across the TM series.

The J_2 superexchange interaction is principally mediated *via* the σ -like and π -like frontier orbitals on $(\text{NCS})^-$, dominated by lobes on S and N atoms [Fig. 10 (b) and (d)]. As with the J_1 interaction, the J_2 interaction comprises both antiferromagnetic and ferromagnetic components. The former arises from delocalisation superexchange, where one t_{2g} and one e_g orbital on each M^{2+} overlap *via* the σ -like frontier orbital on $(\text{NCS})^-$ [Fig. 10(b)]. The latter is a ferromagnetic exchange-correlation driven interaction between the e_g orbitals on M^{2+} , mediated by the orthogonal σ - and π -like frontier orbitals on $(\text{NCS})^-$ [Fig. 10(d)].

As electrons are added to the t_{2g} orbitals on moving from Mn^{2+} to Ni^{2+} , the antiferromagnetic component of the J_2 interaction again weakens and becomes zero for $M = \text{Ni}$, resulting in a more ferromagnetic J_2 . Indeed, for many $M(\text{NCS})_2$ solvate frameworks (those of the form $M(\text{NCS})_2L_x$, where $L = \text{ligand}$), the Ni member of the family orders ferromagnetically along the Ni-NCS-Ni chains, whilst the Mn and Co members order antiferromagnetically,^{18,22,66-68} indicating that the exchange interaction along the M -NCS- M chains

(i.e. the J_2 interaction in the frameworks studied in this work) is ferromagnetic for $M = \text{Ni}$ and antiferromagnetic for earlier M in the series, which is consistent with our experimental results.

Deviations from the 'ideal' 90° and 180° bond angles will likely mix the ferromagnetic and antiferromagnetic components of each interaction, giving deviations from the trends we explain above. Nevertheless, our qualitative predictions of the signs and strengths of the J_1 and J_2 interactions broadly bear out the observed magnetic ground states and trends in the bulk magnetic properties observed.

Our magnetochemical arguments therefore account for the observed increasingly antiferromagnetic interactions in the $M(\text{NCS})_2$ framework with earlier M^{2+} . Our qualitative predictions also allow us to place each compound in the classical two-dimensional magnetic phase diagram [Fig. 2(a)]. For $M = \text{Mn}$, Fe and Co , we expect $J_2 > 0$ (i.e. antiferromagnetic), whilst we expect J_1 to be small and either ferromagnetic or antiferromagnetic, due to cancellation of the superexchange contributions. Therefore, these materials all lie in the AF region of the phase diagram. If J_1 becomes antiferromagnetic, this will

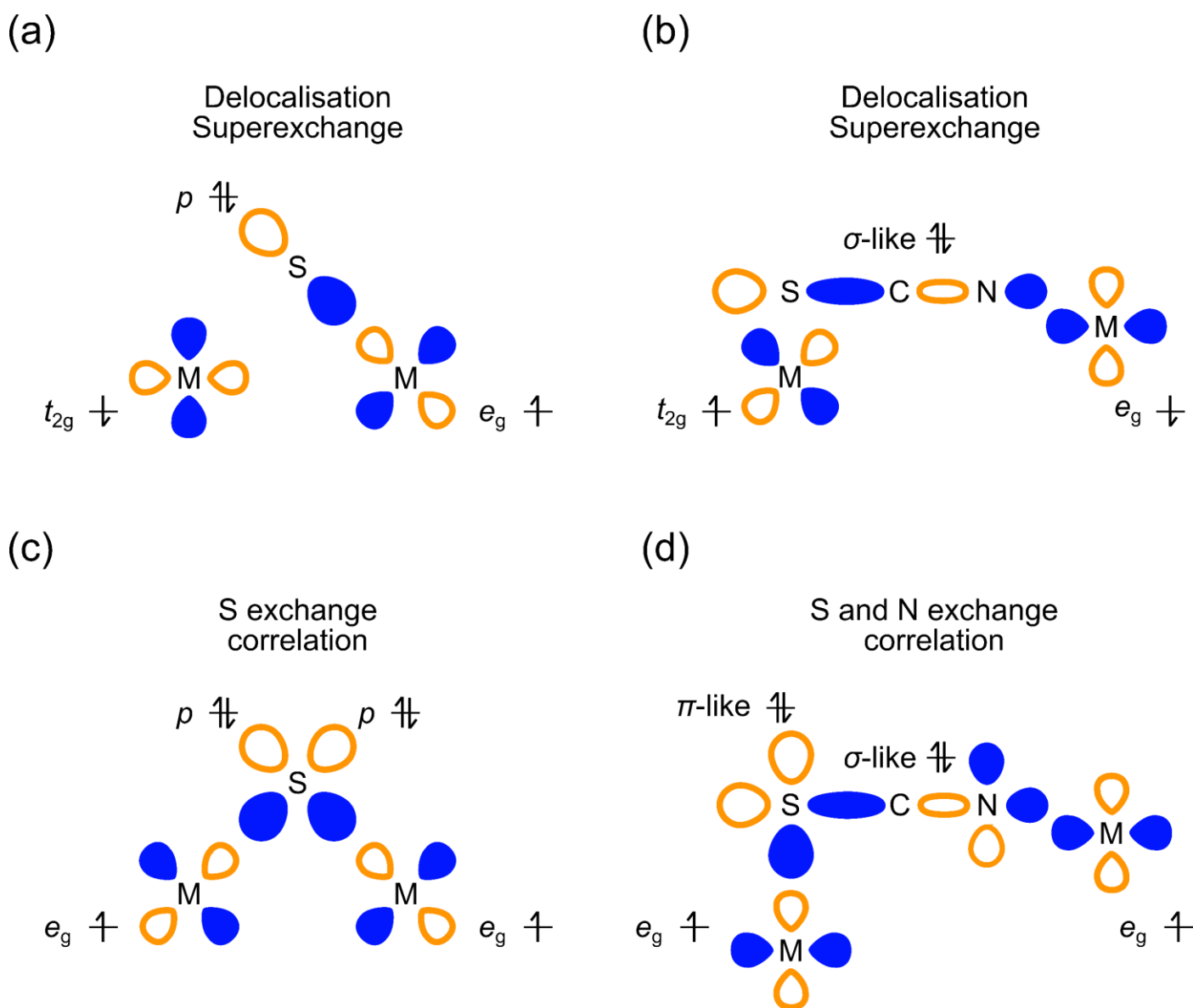


Fig. 10: Schematic figures illustrating simplified superexchange mechanisms for the J_1 ((a) and (c)) and J_2 ((b) and (d)) interactions in terms of the magnetic M^{2+} $3d$ orbitals and frontier σ -like and π -like orbitals on $(\text{NCS})^-$. Orange and blue lobes indicate opposite phases of orbital wavefunctions. The antiferromagnetic components of the J_1 ((a)) and J_2 ((b)) interactions proceed *via* delocalisation superexchange, whilst the ferromagnetic components proceed *via* exchange correlation—either *via* S only for J_1 ((c)) or *via* S and N for J_2 ((d)).

introduce frustration into the lattice. The large

(compared to other M in the series) frustration parameter observed for $\text{Mn}(\text{NCS})_2$ suggests that J_1 may be weakly antiferromagnetic for this compound, and that the larger J_2 interaction, mediated by the $(\text{NCS})^-$ linkages controls the overall antiferromagnetic ordering.

also predict that J_1 has an increasing antiferromagnetic component for earlier M in the series. If J_1 becomes antiferromagnetic, this introduces frustration into the lattice. The relatively large (compared to M in the series) frustration parameter for $\text{Mn}(\text{NCS})_2$ suggests that J_1 may actually be weakly antiferromagnetic for this compound and that the larger J_2 interaction mediated by the $(\text{NCS})^-$ linkages controls the overall antiferromagnetic ordering.

For $M = \text{Ni}$, we anticipate $J_2 < 0$, which places $\text{Ni}(\text{NCS})_2$ in the FM region of the phase diagram, as expected from the observed magnetic ground state. We also expect the J_1 interaction to be ferromagnetic (i.e. $J_1 < 0$).

For all members of the $M(\text{NCS})_2$ family, the size of the staggered moments obtained from PND are all lower than the size of the expected ordered moment (i.e. gS). This likely corresponds to a covalency effect, where spin density is transferred from M^{2+} to the $(\text{NCS})^-$ ligand.⁶⁹ Finally, we find that the ordered moment lies broadly along the N–M–N axis for $\text{Mn}(\text{NCS})_2$ and $\text{Ni}(\text{NCS})_2$, suggesting significant spin density in the d orbital pointing along that axis. For $\text{Fe}(\text{NCS})_2$ and $\text{Co}(\text{NCS})_2$, the moment has a significant tilt away from the N–M–N axis, towards the meridional plane containing S-bound $(\text{NCS})^-$ ligands. This perhaps reflects the less axially symmetric occupancies of the t_{2g} orbitals, compared to Mn^{2+} and Ni^{2+} : where Mn^{2+} and Ni^{2+} have equal occupancies in each t_{2g} orbital, Fe^{2+} and Co^{2+} do not, leading to a more ‘asymmetric’ unpaired spin density distribution. Future electron spin resonance spectroscopy investigations will shed further light on the origin of these differences.

Recent work on CrI_3 and $\text{Cr}_2\text{Ge}_2\text{Te}_6$ has shown that mechanical exfoliation of layered ferromagnets can generate single-layer magnets.^{70,71} Whilst $\text{Ni}(\text{NCS})_2$ is strictly a bulk three-dimensional framework, the presence of ferromagnetic order in the layers with only weak exchange interactions between the layers suggests that it may be possible to retain the bulk magnetic order of $\text{Ni}(\text{NCS})_2$ when reduced to a

single layer, provided that the single ion spin anisotropy is sufficiently large.

If single-layer $\text{Ni}(\text{NCS})_2$ retains the same ordering pattern as the bulk material, these single-layer ferromagnets may have applications as magnetoelectronic devices, ferromagnetic light emitters^{70,71} and hybrid multilayer materials,^{72,73} motivating future synthetic studies.

V CONCLUSION

In this study, we have determined how the strengths of magnetic interactions vary across the first-row TM pseudobinary thiocyanates, $M(\text{NCS})_2$. Two new materials— $\text{Mn}(\text{NCS})_2$ and $\text{Fe}(\text{NCS})_2$ —are reported, alongside the magnetic structures of these materials and of $\text{Co}(\text{NCS})_2$ and $\text{Ni}(\text{NCS})_2$. Based on the observed magnetic structures, we have qualitatively rationalised the relative strengths and signs of the nearest-neighbour in-plane exchange interactions, J_1 and J_2 , and have systematically studied the magnetic phase diagram of the spatially anisotropic triangular lattice.

On moving to TM ions earlier in the row, the net magnetic interactions become stronger and increasingly antiferromagnetic, with the Weiss constant reaching $-115(3)$ K for $\text{Mn}(\text{NCS})_2$.

PND revealed that $\text{Mn}(\text{NCS})_2$, $\text{Fe}(\text{NCS})_2$ and $\text{Co}(\text{NCS})_2$ adopt the same commensurate antiferromagnetic structure, where chains of co-parallel spins along the crystallographic b axis order antiferromagnetically along the a axis, with these layers stacked antiferromagnetically along the c -direction. In contrast, the magnetic structure of $\text{Ni}(\text{NCS})_2$ comprises ferromagnetically ordered layers ordered antiferromagnetically along the c -axis. This suggests that single-layer $\text{Ni}(\text{NCS})_2$ may be a candidate monolayer ferromagnet belonging to a new family of magnetic frameworks. The results collected from this study open up new avenues for the rational design of magnetic molecular framework materials.

Conflicts of Interest

There are no conflicts of interest to declare.

ACKNOWLEDGEMENTS

E.N.B. thanks the EPSRC for financial support. J.A.M.P.'s work at Cambridge was supported by Churchill College, University of Cambridge. J.A.M.P.'s work at ORNL (discussion of magnetic modelling) was supported by ORNL LDRD 10004, and the U.S. Department of Energy, Office of Science, Basic Energy Sciences, Materials Sciences and Engineering Division. E.N.K. thanks NSERC of Canada for a PGSD. J.L. thanks Trinity College, University of Cambridge for financial support. M.J.C. acknowledges the School of Chemistry, University of Nottingham for a Hobday Fellowship. We acknowledge the Rutherford Appleton Laboratory for access to the ISIS Neutron Source. Magnetic measurements were carried out using the Advanced Materials Characterisation Suite, funded by EPSRC Strategic Equipment Grant EP/M000524/1.

NOTES AND REFERENCES

1. Ramesh, R. Emerging routes to multiferroics. *Nature* **461**, 1218–1219 (2009).
2. Stroppa, A., Barone, P., Jain, P., Perez-Mato, J. M. & Picozzi, S. Hybrid improper ferroelectricity in a multiferroic and magnetoelectric metal-organic framework. *Adv. Mater.* **25**, 2284–2290 (2013).
3. Boström, H. L. B., Senn, M. S. & Goodwin, A. L. Recipes for improper ferroelectricity in molecular perovskites. *Nat. Commun.* **9**, 2380 (2018).
4. Wang, Z. *et al.* Dimethylammonium copper formate [(CH₃)₂NH₂]Cu(HCOO)₃: A metal-organic framework with quasi-one-dimensional antiferromagnetism and magnetostriction. *Phys. Rev. B* **87**, 224406-1-224406-8 (2013).
5. Maspoch, D., Ruiz-Molina, D. & Veciana, J. Magnetic nanoporous coordination polymers. *J. Mater. Chem.* **14**, 2713–2723 (2004).
6. Motokawa, N. *et al.* Reversible Magnetism between an Antiferromagnet and a Ferromagnet Related to Solvation/Desolvation in a Robust Layered [Ru 2] 2 TCNQ Charge-Transfer System. *J. Am. Chem. Soc.* **132**, 11943–11951 (2010).
7. Maspoch, D. *et al.* A nanoporous molecular magnet with reversible solvent-induced mechanical and magnetic properties. *Nat. Mater.* **2**, 190–195 (2003).
8. Cliffe, M. J. *et al.* Low-dimensional quantum magnetism in Cu(NCS)₂, a molecular framework material. *Phys. Rev. B* **97**, 144421 (2017).
9. Greenfield, J. T., Kamali, S., Izquierdo, N., Chen, M. & Kovnir, K. NH₄FeCl₂(HCOO): Synthesis, Structure, and Magnetism of a Novel Low-Dimensional Magnetic Material. *Inorg. Chem.* **53**, 3162–3169 (2014).
10. Saines, P. J., Paddison, J. A. M., Thygesen, P. M. M. & Tucker, M. G. Searching beyond Gd for magnetocaloric frameworks: magnetic properties and interactions of the Ln(HCOO)₃ series. *Mater. Horizons* **2**, 528–535 (2015).
11. Kurmoo, M. & Kepert, C. J. Hard magnets based on transition metal complexes with the dicyanamide anion, [N(CN)₂]⁻. *New J. Chem.* **22**, 1515–1524 (1998).
12. Saines, P. J. & Bristowe, N. C. Probing magnetic interactions in metal-organic frameworks and coordination polymers microscopically. *Dalton Transactions* vol. 47 13257–13280 (2018).
13. Landee, C. P. & Turnbull, M. M. Review: A gentle introduction to magnetism: units, fields, theory, and experiment. *J. Coord. Chem.* **67**, 375–439 (2014).
14. Balents, L. Spin liquids in frustrated magnets. *Nature* **464**, 199–208 (2010).
15. Wen, J., Yu, S.-L., Li, S., Yu, W. & Li, J.-X. Experimental identification of quantum spin liquids. *npj Quantum Mater.* **4**, 12 (2019).
16. Lee, P. A., Nagaosa, N. & Wen, X.-G. Doping a Mott insulator: Physics of high-temperature superconductivity. *Rev. Mod. Phys.* **78**, 17–85 (2006).
17. Shurdha, E. *et al.* Extended Network Thiocyanate- and Tetracyanoethanide-Based First-Row Transition Metal Complexes. *Inorg. Chem.* **51**, 9655–9665 (2012).
18. DeFotis, G. C., Harlan, E. W., Remy, E. D. & Dell, K. D. Ferromagnetism of Ni(SCN)₂(C₂H₅OH)₂. *J. Appl. Phys.* **69**, 6004–6006 (1991).
19. Julve, M., Verdaguer, M., De Munno, G., Real, J. A. & Bruno, G. Synthesis, Crystal Structure, and Magnetic Properties of (μ-Bipyrimidine)(cyanato)copper(II) and-(thiocyanato)copper(II) Complexes. *Inorg. Chem.* **32**, 795–802 (1993).
20. Shurdha, E. *et al.* First row transition metal(II) thiocyanate complexes, and formation of 1-, 2-, and 3-dimensional extended network structures of M(NCS)₂(solvent)₂ (M = Cr, Mn, Co) composition. *Inorg. Chem.* **52**, 10583–10594 (2013).
21. Reller, A. & Oswald, H. R. Mechanism and Kinetics of Thermal Decompositions of Solids Governed by Phase-Boundary Processes. *J. Solid State Chem.* **62**, 306–316 (1986).
22. Boeckmann, J. & Näther, C. Metamagnetism and long range ordering in μ-1,3 bridging transition metal thiocyanato coordination polymers. *Polyhedron* **31**, 587–595 (2012).
23. Dhers, S., Feltham, H. L. C. & Brooker, S. A toolbox of building blocks, linkers and crystallisation methods used to generate single-chain magnets. *Coord. Chem. Rev.* **296**, 24–44 (2015).
24. Dubler, E., Reller, A. & Oswald, H. R. Intermediates in thermal decomposition of nickel(II) complexes: The crystal structures of Ni(SCN)₂(NH₃)₂ and Ni(SCN)₂. *Zeitschrift für Krist. - Cryst. Mater.* **161**, 265–278 (1982).

25. DeFotis, G. C., Dell, K. D., Krovich, D. J. & Brubaker, W. W. Antiferromagnetism of Ni(SCN)₂. *J. Appl. Phys.* **73**, 5386–5388 (1993).
26. Paddison, J. A. M. *et al.* Continuous excitations of the triangular-lattice quantum spin liquid YbMgGaO₄. *Nat. Phys.* **13**, 117–122 (2017).
27. Dutton, S. E. *et al.* Helical magnetism and structural anomalies in triangular lattice α -SrCr₂O₄. *J. Phys. Condens. Matter* **23**, 246005 (2011).
28. Damay, F. *et al.* Spin-lattice coupling induced phase transition in the $S = 2$ frustrated antiferromagnet CuMnO₂. *Phys. Rev. B* **80**, 094410 (2009).
29. Ramirez, A. P. Strongly Geometrically Frustrated Magnets. *Annu. Rev. Mater. Sci.* **24**, 453–480 (1994).
30. Tokunaga, Y. *et al.* Multiferroicity in NiBr₂ with long-wavelength cycloidal spin structure on a triangular lattice. *Phys. Rev. B* **84**, 060406 (2011).
31. Kurumaji, T. *et al.* Magnetoelectric responses induced by domain rearrangement and spin structural change in triangular-lattice helimagnets NiI₂ and CoI₂. *Phys. Rev. B* **87**, 014429 (2013).
32. Kurumaji, T. *et al.* Magnetic-Field Induced Competition of Two Multiferroic Orders in a Triangular-Lattice Helimagnet MnI₂. *Phys. Rev. Lett.* **106**, 167206 (2011).
33. Kuindersma, S. R., Sanchez, J. P. & Haas, C. Magnetic and Structural Investigations on NiI₂ and CoI₂. *Phys. B+C* **111**, 231–248 (1981).
34. Schmidt, B. & Thalmeier, P. Quantum fluctuations in anisotropic triangular lattices with ferromagnetic and antiferromagnetic exchange. *Phys. Rev. B* **89**, 184402-1-184402-12 (2014).
35. Cong, P. T. *et al.* Distinct magnetic regimes through site-selective atom substitution in the frustrated quantum antiferromagnet Cs₂CuCl_{4-x}Br_x. *Phys. Rev. B* **83**, 064425 (2011).
36. Coldea, R., Tennant, D. A., Tsvetlik, A. M. & Tyliczynski, Z. Experimental Realization of a 2D Fractional Quantum Spin Liquid. *Phys. Rev. Lett.* **86**, 1335–1338 (2001).
37. Golub, A. M. (Andrii M., Köhler, H. & Skopenko, V. V. (Viktor V. *Chemistry of pseudohalides*. (Elsevier, 1986).
38. Pawley, G. S. Unit-cell refinement from powder diffraction scans. *J. Appl. Crystallogr.* **14**, 357–361 (1981).
39. Rietveld, H. M. Line profiles of neutron powder-diffraction peaks for structure refinement. *Acta Crystallogr.* **22**, 151–152 (1967).
40. Rietveld, H. M. A profile refinement method for nuclear and magnetic structures. *J. Appl. Crystallogr.* **2**, 65–71 (1969).
41. Coelho, A. A. *TOPAS and TOPAS-Academic*: an optimization program integrating computer algebra and crystallographic objects written in C++. *J. Appl. Crystallogr.* **51**, 210–218 (2018).
42. Coelho, A. *TOPAS-Academic: General Profile and Structure Analysis Software for Powder Diffraction Data*. (2007).
43. Bain, G. A. & Berry, J. F. Diamagnetic Corrections and Pascal's Constants. *J. Chem. Educ.* **85**, 532–536 (2008).
44. Chapon, L. C. *et al.* Wish: The New Powder and Single Crystal Magnetic Diffractometer on the Second Target Station. *Neutron News* **22**, 22–25 (2011).
45. Arnold, O. *et al.* Mantid—Data analysis and visualization package for neutron scattering and μ SR experiments. *Nucl. Instruments Methods Phys. Res. Sect. A Accel. Spectrometers, Detect. Assoc. Equip.* **764**, 156–166 (2014).
46. Shannon, R. D. Revised effective ionic radii and systematic studies of interatomic distances in halides and chalcogenides. *Acta Crystallogr. Sect. A* **32**, 751–767 (1976).
47. Cliffe, M. J. *et al.* Strongly coloured thiocyanate frameworks with perovskite-analogue structures. *Chem. Sci.* **10**, 793–801 (2019).
48. Addison, A. W. *et al.* The Hexakis(thiocyanato)ferrate(III) Ion: a Coordination Chemistry Classic Reveals an Interesting Geometry Pattern for the Thiocyanate Ligands. *Eur. J. Inorg. Chem.* **2005**, 2404–2408 (2005).
49. Dinsdale, D. R., Lough, A. J. & Lemaire, M. T. Structure and magnetic properties of an unusual homoleptic iron(III) thiocyanate dimer. *Dalt. Trans.* **44**, 11077–11082 (2015).
50. Rosseinsky, D. R. & Dorrity, I. A. Ligand field parameters and spectra of first-row transition metal dihalides in the solid state. *Coord. Chem. Rev.* **25**, 31–67 (1978).
51. Tauc, J. Optical properties and electronic structure of amorphous Ge and Si. *Mater. Res. Bull.* **3**, 37–46 (1968).
52. Tanabe, Y. & Sugano, S. On the Absorption Spectra of Complex Ions. *J. Phys. Soc. Japan* **9**, 753–766 (1954).
53. Tanabe, Y. & Sugano, S. On the Absorption Spectra of Complex Ions II. *J. Phys. Soc. Japan* **9**, 766–779 (1954).
54. Tanabe, Y. & Sugano, S. On the Absorption Spectra of Complex Ions, III The Calculation of the Crystalline Field Strength. *J. Phys. Soc. Japan* **11**, 864–877 (1956).
55. Figgis, B. N. & Lewis, J. *The magnetic properties of polynuclear transition metal complexes*. *Progress in Inorganic Chemistry* vol. 6 (1964).
56. Lovesey, S. W. Magnetic excitations in FeCl₂. *J. Phys. C Solid State Phys.* **7**, 2049–2059 (1974).
57. Hutchings, M. T. Neutron scattering investigation of magnetic excitations in CoCl₂. *J. Phys. C Solid State Phys.* **6**, 3143–3155 (1973).
58. Johnston, D. C. Magnetic Susceptibility of Collinear and Noncollinear Heisenberg Antiferromagnets. *Phys. Rev. Lett.* **109**, 077201-1-077201-5 (2012).

59. Johnston, D. C. Unified molecular field theory for collinear and noncollinear Heisenberg antiferromagnets. *Phys. Rev. B* **91**, 064427-1-064427–27 (2015).
60. Onsager, L. Crystal Statistics. I. A Two-Dimensional Model with an Order-Disorder Transition. *Phys. Rev.* **65**, 117–149 (1944).
61. Cracknell, A. P., Davies, B. L., Miller, S. C. & Love, W. F. *Kronecker product tables*. (IFI/Plenum, 1979).
62. Gallego, S. V. *et al.* Magnetic symmetry in the Bilbao Crystallographic Server: a computer program to provide systematic absences of magnetic neutron diffraction. *J. Appl. Crystallogr.* **45**, 1236–1247 (2012).
63. Goodenough, J. B. An Interpretation of the magnetic properties of the Perovskite-type mixed crystals $\text{La}(1-x)\text{Sr}(x)\text{CoO}(3-\lambda)$. *J. Phys. Chw. Solids Pergamon Press* **6**, 287–297 (1958).
64. Kanamori, J. Theory of the Magnetic Properties of Ferrous and Cobaltous Oxides, I. *Prog. Theor. Phys.* **17**, 177–196 (1957).
65. Kanamori, J. Theory of the Magnetic Properties of Ferrous and Cobaltous Oxides, II. *Prog. Theor. Phys.* **17**, 197–222 (1957).
66. Wöhlert, S., Fink, L., Schmidt, M. U. & Näther, C. Synthesis and Characterization of New 2D Coordination Polymers based on $\text{Mn}(\text{NCS})_2$ and $\text{Ni}(\text{NCS})_2$ with 1, 2-Bis(4-pyridyl)-ethane as Co-Ligand. *Zeitschrift für Anorg. und Allg. Chemie* **639**, 2186–2194 (2013).
67. DeFotis, G. C., McGhee, E. M., Echols, K. R. & Wiese, R. S. Magnetic and structural properties of $\text{Mn}(\text{SCN})_2(\text{ROH})_2$ compounds. *J. Appl. Phys.* **63**, 3569–3571 (1988).
68. DeFotis, G. C., Wimberly, B. T., Jeffers, R. B., May, W. M. & Owens, T. M. Magnetic behavior of single-crystal $\text{Co}(\text{SCN})_2(\text{CH}_3\text{OH})_2$: Three-dimensional Ising metamagnetism and field-induced spin reorientations. *Phys. Rev. B* **76**, 014419-1-014419–7 (2007).
69. Kmety, C. R. *et al.* Noncollinear antiferromagnetic structure of the molecule-based magnet $\text{Mn}[\text{N}(\text{CN})_2]_2$. *Phys. Rev. B* **62**, 5576–5588 (2000).
70. Huang, B. *et al.* Layer-dependent ferromagnetism in a van der Waals crystal down to the monolayer limit. *Nature* **546**, 270–273 (2017).
71. Gong, C. *et al.* Discovery of intrinsic ferromagnetism in two-dimensional van der Waals crystals. *Nature* **546**, 265–269 (2017).
72. Hornick, C., Rabu, P. & Drillon, M. Hybrid organic–inorganic multilayer materials: influence of π electrons as magnetic media in a series of bridged-layer compounds $\text{M}_2(\text{OH})_{4-x}\text{Ax}/2$ ($\text{M}=\text{Cu}(\text{II})$ or $\text{Co}(\text{II})$, $\text{A}=\text{dicarboxylate anion}$). *Polyhedron* **19**, 259–266 (2000).
73. Rabu, P., Drillon, M., Awaga, K., Fujita, W. & Sekine, T. Hybrid Organic-Inorganic Multilayer Compounds: Towards Controllable and/or Switchable Magnets. in *Magnetism: Molecules to Materials* 357–395 (Wiley-VCH Verlag GmbH & Co. KGaA, 2003). doi:10.1002/9783527620548.ch11a.